PHYSICAL REVIEW C **85**, 055809 (2012)

Definition of a standard neutron field with the ^{7}Li(p, n)^{7}Be reaction

C. Lederer,[1,*] F. Käppeler,[2] M. Mosconi,[3] R. Nolte,[3] M. Heil,[4] R. Reifarth,[5] S. Schmidt,[5] I. Dillmann,[4,6] U. Giesen,[3]
A. Mengoni,[7] and A. Wallner[1]
[1] *University of Vienna, Faculty of Physics, Vienna, Austria.*
[2] *Karlsruhe Institute of Technology (KIT), Institut für Kernphysik, Campus Nord, Karlsruhe, Germany.*
[3] *Physikalisch Technische Bundesanstalt (PTB), Braunschweig, Germany.*
[4] *GSI Helmholtzzentrum für Schwerionenforschung GmbH, Darmstadt, Germany.*
[5] *Goethe University Frankfurt, Frankfurt, Germany.*
[6] *II. Physikalisches Institut, Justus-Liebig-Universität Giessen, Giessen, Germany.*
[7] *International Atomic Energy Agency, Nuclear Data Section, Vienna, Austria.*
(Received 30 January 2012; published 29 May 2012)

The quasistellar neutron spectrum for a thermal energy of $kT = 25$ keV that can be produced via the ^{7}Li(p,n)^{7}Be reaction at a proton energy of $E_p = 1912$ keV has been measured using the dedicated setup for the definition of neutron fields at Physikalisch-Technische Bundesanstalt Braunschweig. The results confirm previous work with improved accuracy and resolution. Small variations in proton energy leave the spectrum essentially unchanged. This is illustrated by the example of the (n,γ) cross section of ^{197}Au, where the averaged cross section for the spectrum defined in this work agrees perfectly with the result of a previous measurement.

DOI: 10.1103/PhysRevC.85.055809 PACS number(s): 25.40.Kv, 26.20.Kn, 28.20.−v, 29.20.−c

I. INTRODUCTION

The ^{7}Li(p,n)^{7}Be reaction represents the most prolific neutron source in the kiloelectron-volt region and has been extensively used in a large number of neutron cross-section measurements, predominantly for nucleosynthesis studies in astrophysics but also as an independent check of important cross sections for technological applications.

With respect to astrophysics this reaction became particularly important because it can be used to mimic the stellar neutron spectrum for a thermal energy of $kT = 25$ keV [1], right in the temperature range between 250 and 300 MK, where stellar nucleosynthesis by the slow neutron capture process (s process) takes place [2,3]. Due to this unique feature, effective stellar (n,γ) cross sections, the so-called Maxwellian averaged cross sections (MACS), can be measured directly by activation. Such measurements are important for establishing a complete and reliable set of MACSs data, which are the essential nuclear physics input of comprehensive model calculations characterizing the s-process abundance component, which contributes about half the observed abundances between Fe and Bi [4].

The possibility to simulate the stellar environment has been used in a large number of activation experiments (e.g., Refs. [5,6]) covering the entire periodic table [7]. Simulations of quasistellar spectra have been also obtained for $kT = 5$ [8] and 52 keV [9] using the (p,n) reactions on ^{18}O and ^{3}H, but with significantly reduced intensities. All measurements with this technique were performed relative to the ^{197}Au(n,γ) cross section and rely on the verification of this "quasistellar" spectrum as well as on the fact that the gold cross section has been determined for this spectrum with an accuracy of 1.4% [1].

The results obtained with activation measurements in the quasistellar spectrum depend on a careful measurement of the induced activities, but also on the accurate definition of the neutron spectrum itself. This second problem clearly affects also the value of the gold cross section measured in that spectrum and touches the question of whether the ^{197}Au(n,γ) cross section could be considered as a standard in such applications [10].

This work is intended to check and to solidify existing information [1,11] concerning the quasistellar neutron field produced by the ^{7}Li(p,n)^{7}Be reaction at a proton energy of $E_p = 1912$ keV. In parallel, a very similar study has been performed by Feinberg *et al.* [12]. Measurement and data analysis are presented in Secs. II and III. The results are presented in Sec. IV and possible implications for the extension of the gold standard cross section to the energy range below 200 keV are discussed in Sec. V.

II. MEASUREMENT

The experiment was performed at the Ion Accelerator Facility (PIAF) at Physikalisch-Technische Bundesanstalt Braunschweig (PTB) [13]. The low-scatter facility for the production of neutron reference fields in open geometry was perfectly suited for the purpose of the present measurement and can be used without further modifications. The particular advantage of this facility (shown in the upper left corner of Fig. 1) is the large open pitch around the neutron target in the center. In this way background from scattered neutrons is reduced significantly.

The proton beam for neutron production was delivered by the PTB pulsed 3.75 MV Van de Graaff accelerator with a repetition rate of 625 kHz, a nominal pulse width of 1.5 ns, a nominal energy of 1912 ± 1.2 keV, and an average current of 0.5–0.8 μA. The lithium target in the center of the spectrometer

---

[*] Corresponding author: claudia.lederer@univie.ac.at

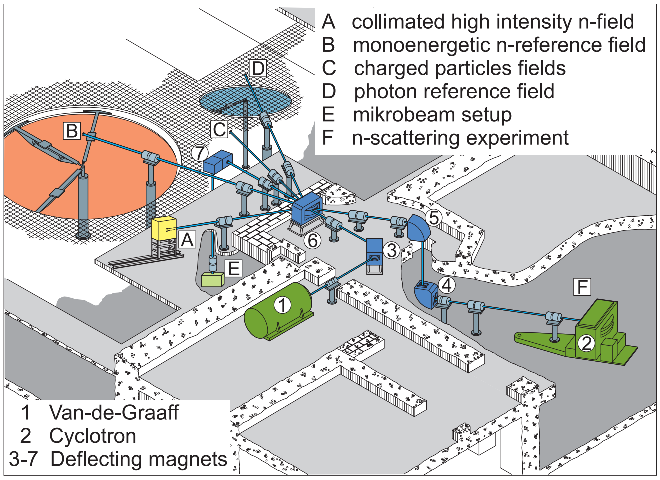

FIG. 1. (Color online) The Ion Accelerator Facility (PIAF) at PTB Braunschweig. The low-scatter facility for the production of neutron reference fields in the upper left corner is designed with an open pitch around the central neutron target to minimize background from scattered neutrons [14].

(position B in Fig. 1) was prepared by vapour deposition of a metallic lithium layer 25 mm in diameter on a tantalum backing 0.5 mm in thickness. The target thickness of 10 μm (564 μg/cm^2) was sufficient to slow all protons down below the threshold of the ^{7}Li$(p,n)^7$Be reaction at 1881 keV for obtaining a reproducible and well-defined neutron field.

The target was mounted on the beam line without breaking the vacuum to protect the Li layer from oxidation. To reduce the heat load to the lithium layer, the target was rotated during the measurements at a speed of 1 rotation per second such that the beam spot described a circle about 6 mm in diameter. The target was cooled by a jet of cold air to avoid the moderating influence of cooling water. The neutron yield decreased almost linearly by only 4.8% during the four days of the experiment as indicated in Fig. 2. A low-mass target assembly was used to minimize the effect of neutron scattering in the target surroundings.

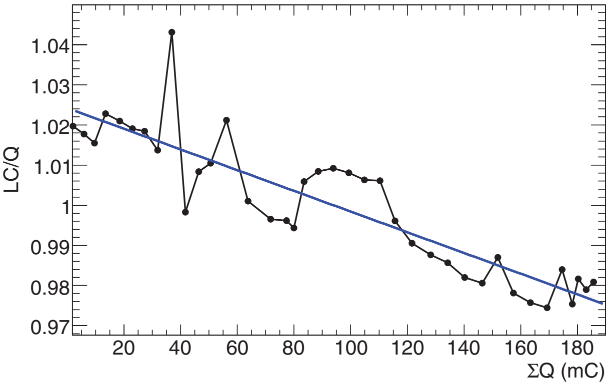

FIG. 2. (Color online) Ratio of the long counter readings (LC) and the accumulated beam charge (Q) for the individual runs as a function of the total accumulated beam charge (ΣQ). During the experiment a decrease of neutron yield by about 4.8% was observed due to target degradation. The data are fitted with a linear function $a_0 + a_1 \times \Sigma Q$.

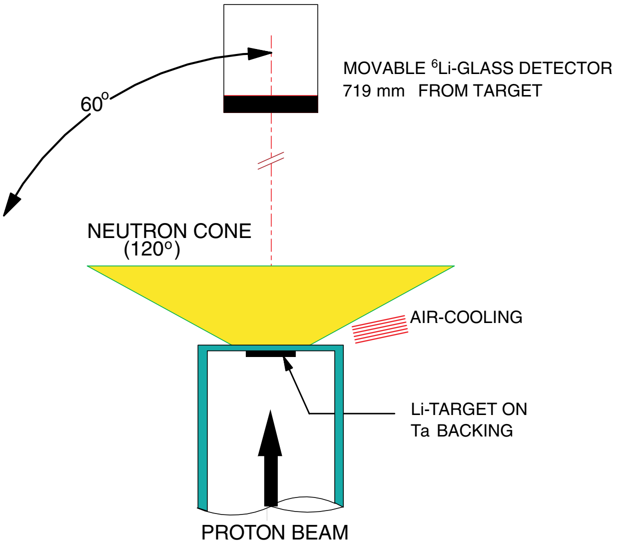

FIG. 3. (Color online) Schematic sketch of the experimental setup, showing the air-cooled Li target, the 0.5-mm thick Ta backing, and the forward peaked neutron field obtained with the ^{7}Li$(p,n)^7$Be reaction at $E_p = 1912$ keV [1].

Because the proton energy is chosen only 31 keV above the reaction threshold, the center-of-mass velocity of the ^{8}Be* produced in the reaction still exceeds the speed of the subsequently emitted neutrons. Accordingly, the resulting neutron field is restricted to a forward cone with 120° opening angle as sketched in Fig. 3. This feature is important for the astrophysical application because a sample directly in front of the neutron target at the point of highest flux is fully exposed to the quasistellar spectrum for $kT = 25$ keV that is obtained by integration over the entire neutron cone. Figure 3 shows also that cooling is achieved by radial heat conduction to avoid moderation by the water.

Neutron spectra were recorded using a ^{6}Li-glass detector mounted on the arm of the spectrometer B that can be rotated around the neutron target in the center of an open pitch (upper left corner of Fig. 1). With the movable detector the angular range between 0° and 65° was covered in steps of 5°. The ^{6}Li-glass scintillator was 38.9 mm in diameter and 2.85 mm in thickness and had a density of 2.405 g/cm^3. The detector was directly coupled to the window of an XP2020 photomultiplier and covered with a lightweight can made of stainless steel. The entrance window of this can had a thickness of 0.25 mm. A stationary long counter mounted at an angle of $-17°$ about 6 m from the neutron target was used to monitor the neutron yield of the Li target throughout the entire experiment. The statistical uncertainties of the resulting normalization factors were negligibly small. The relative standard deviation of the individual long counter readings per unit beam charge was 0.8%, demonstrating the stability of the monitoring procedure (see Fig. 2). This figure shows also a slight decrease of 4.8% in neutron yield due to target degradation effects.

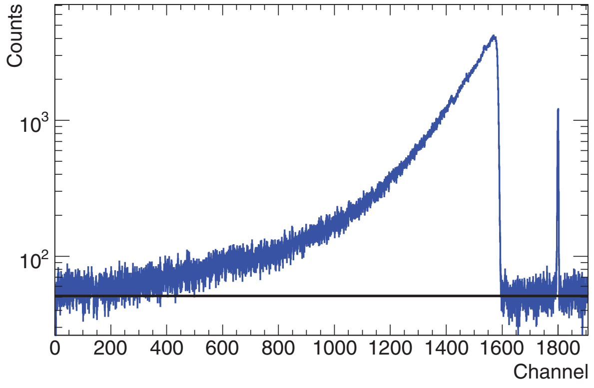

FIG. 4. (Color online) Time-of-flight spectrum taken at a flight path of 719 mm and a neutron angle of 25° relative to the direction of the proton beam. The full width at half maximum (FWHM) of the γ peak and the width of the TOF channels were 3 and 0.83 ns, respectively. The flat background is defined in the region between γ peak and onset of the neutron distribution (channels 1800 and 1600).

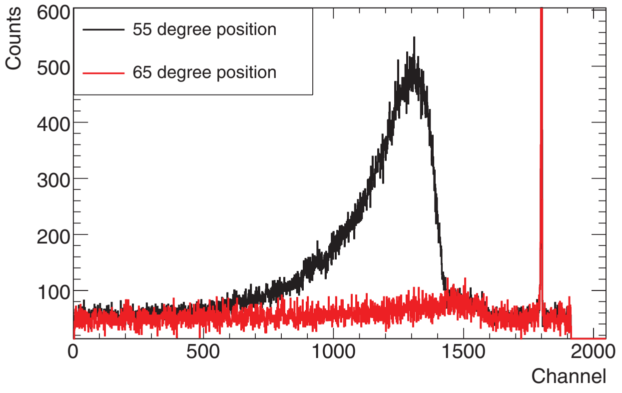

FIG. 6. (Color online) TOF spectra taken at 55° and 65°. The 65° spectrum, where the detector was already outside the direct neutron beam (lower red curve), was used for correcting the background due to neutrons scattered in the target backing. The 65° and 55° spectra shown in the figure were measured a flight path of 719 mm.

The data were accumulated in two-dimensional spectra consisting of 2048 time-of-flight (TOF) versus 1024 pulse height channels. The total time resolution of the experiment was 3.0 ns FWHM, which includes the time spread of the proton beam pulses and the time resolution of the ^{6}Li-glass detector.

In a first series of runs the ^{6}Li-glass detector was mounted at an effective flight path of 719 mm between the target and the center plane of the scintillator. Measuring times varied between about 1.5 and 3 h to compensate for the decrease in intensity with increasing emission angle. The stability of the system was checked twice a day by reference measurements at 0°.

In a second series of runs the flight path was reduced to 369 mm. By using the same measuring times as before the signal/background ratio at the lower energy end of the spectrum could be considerably improved. The different flight paths were also useful to check whether the background in the TOF spectra was really flat or whether corrections, for instance for inscattering of neutrons, had to be considered. Such effects, which would give rise to inconsistencies in the spectral shapes, were also studied in dedicated background runs by using a blank target without any lithium. None of these tests showed detectable indications for hidden backgrounds (see below). Additional control runs were performed with targets, which consisted of LiF layers, using 565 and 550 μg/cm^2 in thickness, evaporated onto Ta and Ag backings, respectively.

The quality of the TOF measurements is illustrated in Fig. 4, which shows the spectrum at 25° taken at a flight path of 719 mm. The 3.0 ns resolution in TOF is determined by the sharp γ peak at channel 1800. The background level was reduced by setting a pulse height threshold in the minimum between neutron-induced signals and the low-energy part of the distribution containing mostly low-energy γ events and electronic noise as illustrated in the pulse height spectrum of Fig. 5.

The repetition rate was low enough that corrections due to the overlap of successive neutron bursts were negligibly small. Therefore, a time-independent background was defined in the

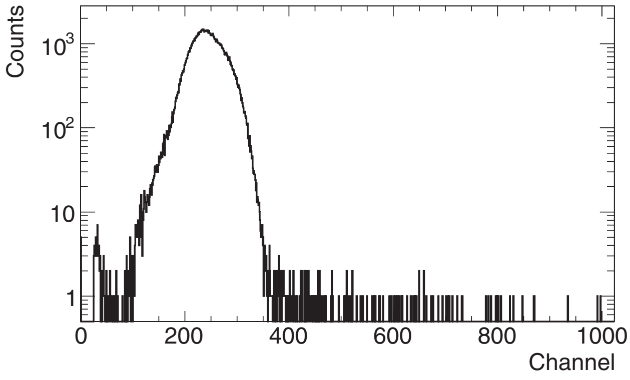

FIG. 5. Pulse height spectrum showing the separation between neutron events and background. Most of the γ signals are suppressed by the pulse height threshold.

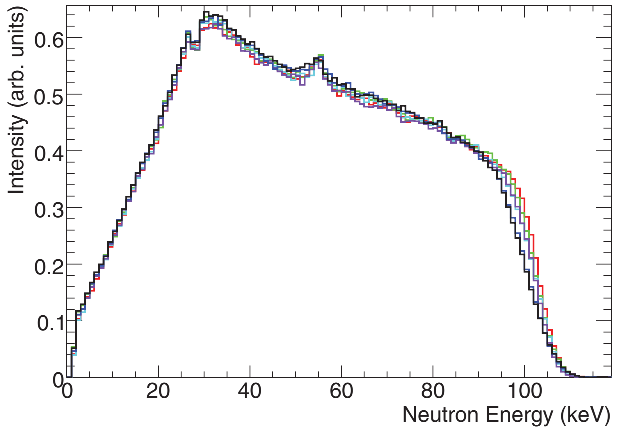

FIG. 7. (Color online) Reference runs recorded in regular intervals throughout the experiment. The loss of high-energy neutrons observed in later runs is due to target degradation effects. Most likely, thin carbon layers were deposited on the target surface which reduced the energy of the protons entering the lithium layer.

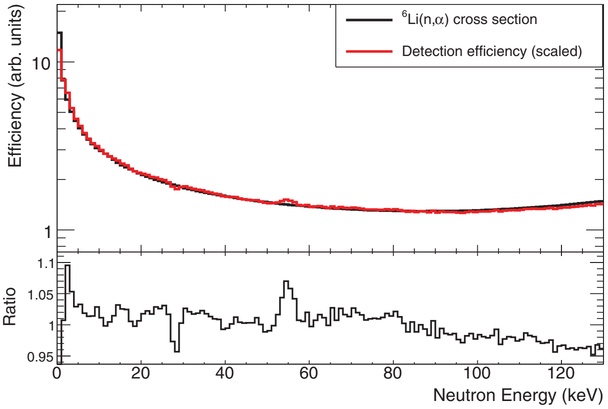

FIG. 8. (Color online) Monte Carlo simulation of the detector efficiency with the GEANT3 code compared to the efficiency exclusively based on the ^{6}Li$(n, \alpha)^3$H cross section. The ratio of the two curves is shown in the lower panel.

region between the γ peak and the onset of the neutron distribution (near channel 1600 in the example of Fig. 4). The assumption of a constant background was justified because a significant structure in the TOF background underneath the neutron distribution in Fig. 4 would have caused corresponding differences in the neutron spectra measured at 719 and 369 mm.

III. DATA ANALYSIS

A dead time correction was applied by means of the real and live time ratio determined by the data acquisition system. This correction was never exceeding 1% and had negligible impact on the data. The flat background defined in the region between γ peak and onset of neutron events was subtracted.

At larger angles, intensities are decreasing and the maximum neutron energy is expected to decrease as well. The TOF spectra acquired in this angular range were found to show a feature on the high-energy side, independent of the angle. This background component, which was attributed to neutron scattering in the target, can be determined by the spectrum at 65°, where the detector was already outside of the direct neutron beam. The effect is illustrated in Fig. 6 by comparison with the 55° and 65° spectra taken at a flight path of 719 mm. This scattering background was eliminated by subtraction of the 65° spectrum (scaled for the respective fluence).

After transformation to an energy grid the histograms were rebinned in the region from 0 to 120 keV with bin widths of 0.5 and 1 keV, respectively. The uncertainty of the background and dead time corrected spectrum per bin is

$$\sigma = \sqrt{\left(\frac{C}{\sqrt{C'}}\right)^2 + \sigma_{\mathrm{bg}}^2}, \qquad (1)$$

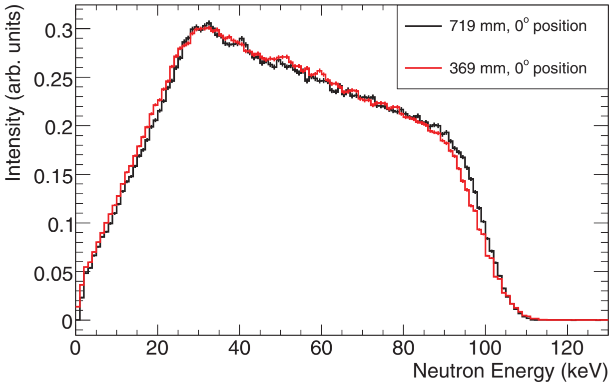

FIG. 9. (Color online) Comparison of the neutron spectra taken at 0° at flight paths of 369 cm and 719 mm. The very good agreement justifies the assumption of a flat TOF background in data analysis.

where C refers to the dead time corrected spectrum without background subtraction, C' to the raw spectrum, and σ_{bg} denotes the uncertainty of the background components due to neutron scattering in the experimental area (flat background) and due to neutron scattering in the target.

The efficiency of the ^{6}Li-glass detector is essentially determined by the cross section of the ^{6}Li$(n, \alpha)^3$H reaction. However, after conversion of the TOF spectra to a neutron energy scale, structures appeared at 28 and 55 keV, which can be attributed to the 27.8 and 55.67 keV resonances in ^{56}Fe and ^{28}Si, respectively. These features are clearly visible in the reference spectra taken at 0°, which were acquired in regular intervals to verify the stability of the system (Fig. 7). The effect of structural materials in the setup has, therefore, been considered by means of Monte Carlo simulations using a detailed model of the detector as input for the code GEANT3 [15]. The simulated efficiency is compared in Fig. 8 with the respective curve based only on the ^{6}Li$(n, \alpha)^3$H cross section [16].

To obtain the angle integrated neutron spectrum, each spectrum has been scaled by the respective solid angle. For angles $\alpha > 0°$ the corresponding factors

$$f_\alpha = (\cos(\alpha - 2.5°) - \cos(\alpha + 2.5°))/(1 - \cos(60° + 2.5°)), \qquad (2)$$

and for the 0° position

$$f_0 = (1 - \cos(2.5°))/(1 - \cos(60° + 2.5°)) \qquad (3)$$

are listed in Table I.

Figure 9 presents a comparison of the neutron spectra at 0°, which were measured in subsequent runs at the two flight paths of 719 and 369 mm. The spectra are in very good agreement, apart from small differences at the high-energy part, which are due to the different broadening by the time resolution. This

TABLE I. Scaling factors considering the solid angle of the individual angular positions.

Angle	0°	5°	10°	15°	20°	25°	30°	35°	40°	45°	50°	55°	60°
f_α	0.00177	0.01413	0.02815	0.04195	0.05543	0.06850	0.08104	0.09296	0.10418	0.11461	0.12416	0.13277	0.14036

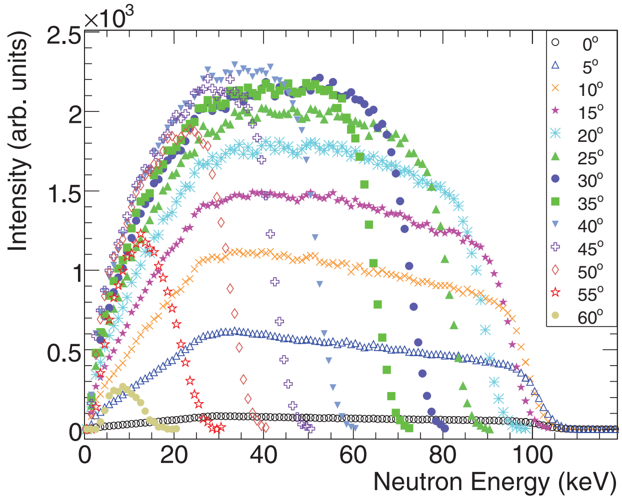

FIG. 10. (Color online) Neutron spectra from 0° to 60° in steps of 5°. Spectra are corrected for the respective solid angle.

consistency justifies the assumption of a flat background in the TOF spectra mentioned before.

IV. RESULTS

The spectra for the measured emission angles are plotted in Fig. 10. The largest part of the integrated spectrum is contributed by the angular range from 25° to 45°. Numerical values of all spectra with a bin width of 1 keV can be found in the EXFOR data base (http://www-nds.iaea.org/exfor/exfor.htm).

The spectrum is given in Table II with a bin width of 0.5 and 1 keV below and above 10 keV, respectively. Above 40 keV the bin width is smaller than the neutron energy resolution of the experiment, which is reaching 4% at 100 keV. The smallest accessible energy is determined by the repetition rate of the accelerator and was 1.2 keV for the 719-mm flight path. The energy range can be extended down to 0.3 keV by normalizing the spectrum obtained at the shorter flight path in the energy range between 1.5 and 3.5 keV. This affects only the first three entries in Table II.

The values of N_E for the angle-integrated neutron spectrum are listed in Table II together with their statistical uncertainties. Additional systematic uncertainties of 2.9% are due to the simulated detection efficiency including the contribution by the ^{6}Li(n,α)^{3}H cross section, and due to the scaling factors

TABLE II. Angle-integrated neutron spectrum obtained from the ^{7}Li(p,n)^{7}Be reaction at 1910 ± 1.2 keV proton energy (derived from the measured TOF spectra). Uncertainties given are statistical. The systematic uncertainty is 2.9%.

E_n (keV)	N_E ($\times 10^{-6}$)	E_n (keV)	N_E ($\times 10^{-6}$)	E_n(keV)	N_E($\times 10^{-6}$)	E_n (keV)	N_E ($\times 10^{-6}$)
0.3–0.5	863 ± 24	21–22	15657 ± 67	52–53	12116 ± 63	83–84	4481 ± 35
0.5–1.0	1204 ± 34	22–23	15977 ± 68	53–54	11651 ± 60	84–85	4096 ± 34
1.0–1.5	1994 ± 56	23–24	16083 ± 68	54–55	11591 ± 60	85–86	3982 ± 34
1.5–2.0	2913 ± 86	24–25	16465 ± 69	55–56	11451 ± 60	86–87	3712 ± 32
2.0–2.5	3836 ± 79	25–26	16787 ± 70	56–57	11005 ± 59	87–88	3525 ± 30
2.5–3.0	5284 ± 74	26–27	16888 ± 72	57–58	11088 ± 60	88–89	3339 ± 29
3.0–3.5	5484 ± 76	27–28	17045 ± 74	58–59	10819 ± 60	89–90	3019 ± 27
3.5–4.0	5889 ± 76	28–29	16715 ± 75	59–60	10607 ± 59	90–91	2799 ± 27
4.0–4.5	6672 ± 77	29–30	16467 ± 73	60–61	10616 ± 60	91–92	2541 ± 26
4.5–5.0	7083 ± 75	30–31	16414 ± 71	61–62	10425 ± 58	92–93	2348 ± 25
5.0–5.5	7671 ± 75	31–32	16397 ± 71	62–63	10122 ± 57	93–94	2133 ± 23
5.5–6.0	8049 ± 75	32–33	16416 ± 72	63–64	9760 ± 56	94–95	1917 ± 22
6.0–6.5	8484 ± 77	33–34	16316 ± 72	64–65	9650 ± 56	95–96	1696 ± 21
6.5–7.0	8883 ± 77	34–35	16024 ± 72	65–66	9126 ± 53	96–97	1454 ± 21
7.0–7.5	9055 ± 78	35–36	15734 ± 72	66–67	9047 ± 54	97–98	1200 ± 19
7.5–8.0	9680 ± 79	36–37	15686 ± 72	67–68	8623 ± 52	98–99	977 ± 17
8.0–8.5	9930 ± 79	37–38	15360 ± 71	68–69	8313 ± 51	99–100	762 ± 16
8.5–9.0	10187 ± 79	38–39	15233 ± 71	69–70	8082 ± 50	100–101	561 ± 16
9.0–9.5	10567 ± 79	39–40	15269 ± 72	70–71	7764 ± 48	101–102	415 ± 14
9.5–10.0	10995 ± 79	40–41	15097 ± 72	71–72	7592 ± 48	102–103	276 ± 14
10–11	11657 ± 57	41–42	14801 ± 71	72–73	7185 ± 47	103–104	173 ± 13
11–12	12385 ± 59	42–43	14232 ± 69	73–74	6843 ± 46	104–105	108 ± 13
12–13	12890 ± 60	43–44	14113 ± 69	74–75	6488 ± 44	105–106	64 ± 13
13–14	13269 ± 60	44–45	13846 ± 69	75–76	6341 ± 43	106–107	39 ± 13
14–15	13415 ± 61	45–46	13589 ± 68	76–77	6116 ± 42	107–108	20 ± 12
15–16	14113 ± 62	46–47	13304 ± 67	77–78	5852 ± 42	108–109	$9\,^{+13}_{-9}$
16–17	14154 ± 63	47–48	13082 ± 66	78–79	5640 ± 40	109–110	$10\,^{+11}_{-10}$
17–18	14765 ± 65	48–49	12979 ± 66	79–80	5504 ± 40	110–111	$8\,^{+12}_{-8}$
18–19	15120 ± 66	49–50	12934 ± 66	80–81	5195 ± 38	111–112	$4\,^{+12}_{-4}$
19–20	15337 ± 67	50–51	12746 ± 66	81–82	4990 ± 37	112–113	12 ± 12
20–21	15482 ± 67	51–52	12537 ± 65	82–83	4753 ± 36	113–114	$2\,^{+12}_{-2}$

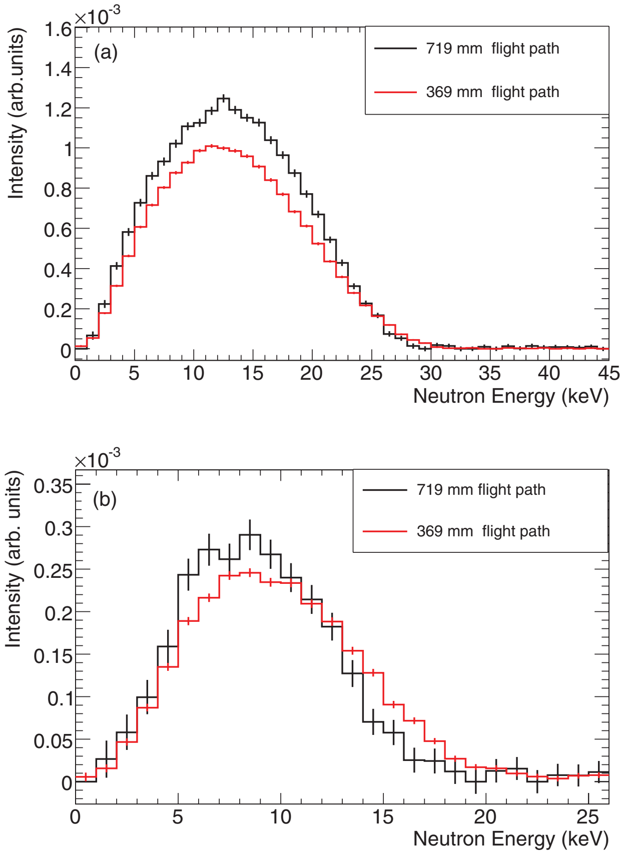

FIG. 11. (Color online) Comparison of the spectra recorded at an angular position of (a) 55° and (b) 60° for the two different flight paths to illustrate the broadening effect due to the different coverage of the solid angle at flight paths of 719 and 369 mm.

f_α. The 0.8% uncertainty of the neutron fluence provided by the long counter (Sec. II) has a negligible impact on the total systematic uncertainty.

The ^{6}Li(n,α)^{3}H cross section is specified with an accuracy ranging from 0.14% at 1 keV to 0.4% at 120 keV [16]. A detection efficiency proportional to the ^{6}Li(n,α) standard cross section deviates between −5% to +5% from the realistic detection efficiency determined by the GEANT3 simulations as shown in Fig. 8. Assuming a 20% uncertainty of the respective corrections including the contribution by the ^{6}Li(n,α)^{3}H cross section, yields a total uncertainty of 2% for the detection efficiency.

The scaling factors f_α were calculated for the geometry of the setup and correspond to the solid angle defined by each of the 5° steps of the measurement. For the longer flight path only about 2/3 of the respective solid angle was covered by the ^{6}Li glass detector, whereas the detector was slightly overlapping the angular positions at the shorter flight path. The resulting differences are most pronounced in the spectra at 55° and 60° and leads to somewhat broader distributions for the shorter flight path as shown in Fig. 11. However, these differences are barely visible in forward direction (Fig. 9), presumably because the distribution is also slightly broadened by the extended beam spot, which was about 3 mm in diameter. In summary, the angle-integrated spectrum is only marginally affected by the experimental coverage of the solid angle. Accordingly, the contribution of the scaling factors f_α to the uncertainty of N_E is less than 2%.

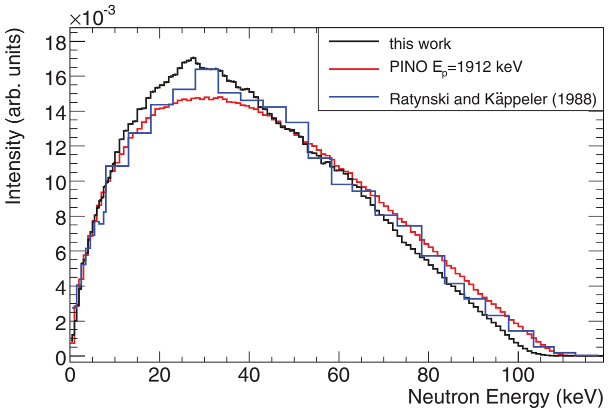

FIG. 12. (Color online) Angle-integrated spectrum compared to the histogram reported by Ratynski and Käppeler [1] and a calculation using the code PINO.

In Fig. 12, the present quasistellar spectrum is compared with the histogram of Ratynski and Käppeler [1] and with an example for a calculated spectrum using the code PINO [17], which generates spectra for the ^{7}Li(p,n)^{7}Be reaction (http://exp-astro.physik.uni-frankfurt.de/pino/). An alternative, less specialized code for neutron spectrum calculations is DROSG-2000 (http://www-nds.iaea.org/drosg2000.html). The spectra in Fig. 12 are normalized to unit area.

In general there is good agreement for the spectra in Fig. 12. The difference between the present results and the PINO calculation indicates that the proton energy in the experiment was around 1910 keV rather than the nominal 1912 keV. In particular, the high-energy tail of the distribution is a very sensitive indicator of the highest proton energies in the lithium layer. The deviation of the experimental and the nominal proton energy can be due to the calibration of the voltage stabilisation system of the Van de Graaff accelerator or due to a small energy loss in a thin additional layer on top of the lithium layer.

A follow-up code of PINO, which includes also angular distribution in the entrance and exit channel, is called N17 and is currently under development [18]. First results are presented in Fig. 13, which illustrates a comparison of the measured angular spectra with a simulation assuming proton energies of 1909 and 1910 keV. The small structures in the neutron distribution at medium energies are the result of the numerical interpolation of remaining uncertainties in the ^{7}Li(p,n) cross section very close to the threshold.

The deviation of the proton energy from the nominal energy of 1912 keV is still compatible with the uncertainty quoted for the energy calibration of the accelerator. A similar but less pronounced difference is seen with respect to the spectrum in Ref. [1], which confirms the small mismatch of the proton energy in the present data.

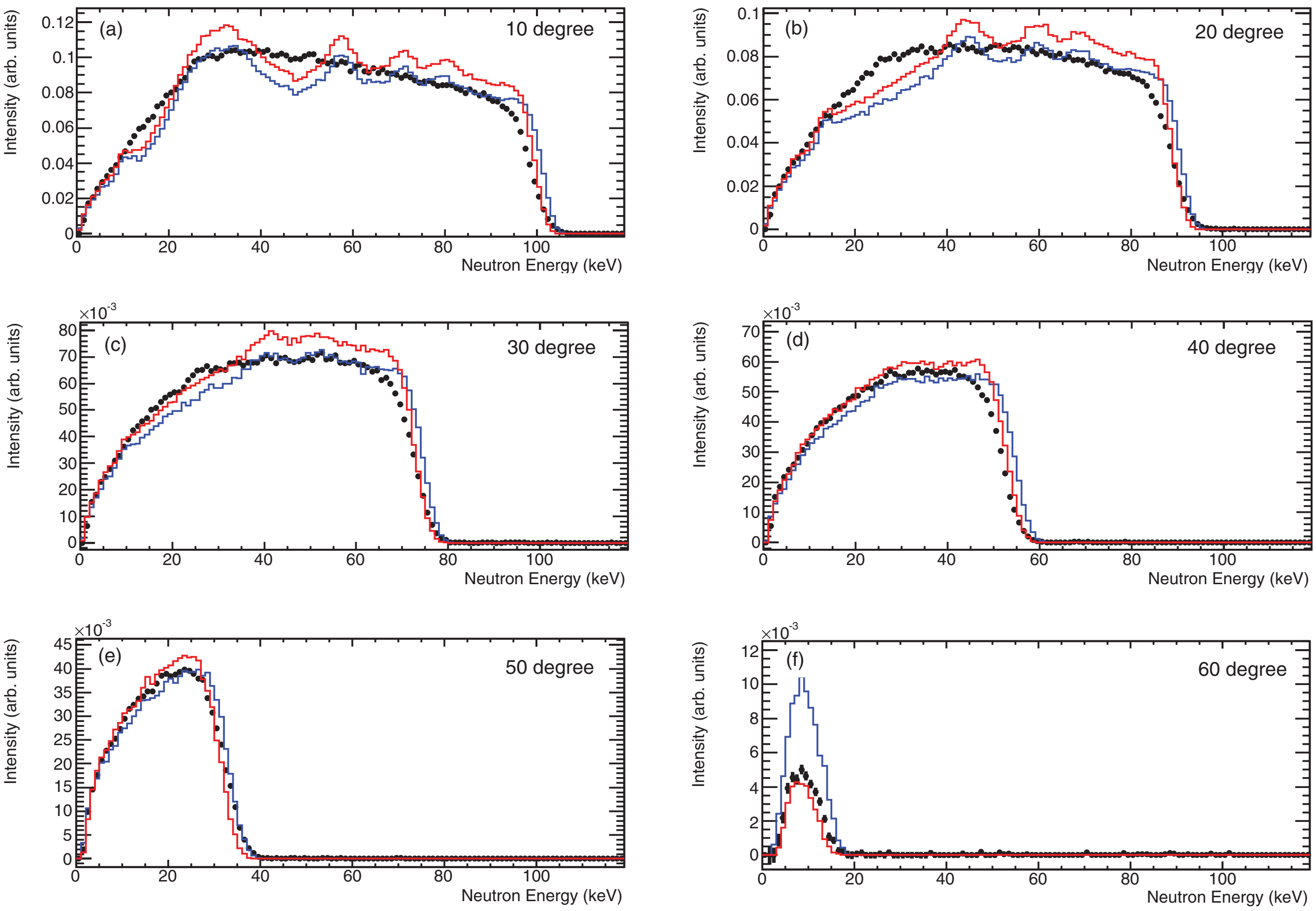

FIG. 13. (Color online) (a–f) Measured angular spectra at a flight path of 719 mm (black dots) compared to calculations using a proton energy of 1909 keV (red) and 1910 keV (blue).

V. IMPLICATIONS FOR THE (n, γ) CROSS SECTION OF ^{197}Au

Standard and reference cross sections play a key role in cross section measurements of neutron-induced reactions. The criteria for cross section standards are (i) that they are smoothly varying with neutron energy (i.e., that their values depend only slightly on experimental resolution), (ii) that they are convenient to use in measurements, and (iii) that they have been determined by absolute techniques and with high accuracy of 1–3%. So far, the (n, γ) cross section of ^{197}Au is recommended as a standard at thermal neutron energies and between 0.2 and 2.5 MeV [19].

Reference cross sections are cases that are particularly useful for specific measurements, but do not meet all criteria of a standard (i.e., because of fluctuations with neutron energy due to overlapping resonances). The neutron capture cross section of ^{197}Au represents such an example. Apart from cross section fluctuations below about 20 keV, there are a number of attractive features, which make it desirable to extend the energy range, where the $^{197}\mathrm{Au}(n, \gamma)$ cross section can be used as a standard. Gold is an element with a single stable isotope, it is easily available in large amounts and with high purity, and has a conveniently large capture cross section.

For these reasons gold has already been used as a reference in numerous (n, γ) cross section measurements at keV neutron energies. This holds in particular for applications in nuclear astrophysics [7], where the capture cross sections of the stable isotopes between ^{12}C and ^{209}Bi represent the key ingredients for describing stellar nucleosynthesis by the slow neutron capture process (s process) between Fe and Bi.

The present measurement of the quasistellar spectrum for $kT = 25$ keV confirms the definition of the neutron field used in Ref. [1], thus supporting the accurate absolute capture cross section obtained in that activation experiment. In this context it is particularly important that a slight mismatch in proton energy has only a very small effect on the gold cross section. This is demonstrated by calculating the spectrum averaged (n, γ) cross section of Au using the evaluated Au cross section from the ENDF/B-VII library (http://www.nndc.bnl.gov/exfor/endf.htm). The results are 636.6 and 632.6 mb for the present spectrum and for that of Ref. [1], corresponding to an almost negligible difference of 0.6%. Using the calculated spectra with PINO at proton energies of 1909 and 1912 keV, one finds a difference of 1.8% for the spectrum averaged cross section, still compatible with the 1.4% uncertainty claimed for the gold cross section in the quasistellar spectrum. The robustness of this test strongly confirms the accuracy that can be obtained in activation measurements as claimed by the authors of Ref. [1].

The role of the gold cross section as a potential standard in such activations seems, however, not yet settled. The 5.5% discrepancy of the spectrum-averaged gold cross section obtained with the the ENDF/B-VII evaluation and measured in the activation of Ref. [1] could not be resolved. Recent TOF measurements at the n_TOF facility at CERN [20] led to a cross section more consistent with the ENDF/B-VII library. The n_TOF data are, however, within uncertainties, still compatible with the activation result of Ref. [1]. Similar results have been reported from the Geel Linear Accelerator (GELINA) in Geel [21,22].

Whether the differences between activation and TOF measurements can be attributed to possible uncertainties of the prompt γ-ray technique (i.e., to variations of the capture γ-ray spectrum with neutron energy or to enhanced internal conversion effects in the capture γ cascades of ^{197}Au [23]) needs to be clarified and will be crucial for accepting the (n,γ) cross section of ^{197}Au as a capture standard for the keV region.

ACKNOWLEDGMENTS

We would like to thank M. Thiemig for the preparation of the Li targets and the PTB accelerator team O. Döhr, H. Eggestein, T. Heldt, and M. Hofmann for the excellent beam conditions and the continuous help during the entire experiment. This work was partly supported by the Austrian Science Fund (FWF), Projects P20434 and I428, by the European Commission within the Sixth Framework Programme through I3-EFNUDAT (EURATOM Contract No. 036434), and by the German Israely Foundation (GIF).

[1] W. Ratynski and F. Käppeler, Phys. Rev. C **37**, 595 (1988).

[2] R. Gallino, C. Arlandini, M. Busso, M. Lugaro, C. Travaglio, O. Straniero, A. Chieffi, and M. Limongi, Astrophys. J. **497**, 388 (1998).

[3] M. Busso, R. Gallino, and G. Wasserburg, Ann. Rev. Astron. Astrophys. **37**, 239 (1999).

[4] C. Arlandini, F. Käppeler, K. Wisshak, R. Gallino, M. Lugaro, M. Busso, and O. Straniero, Astrophys. J. **525**, 886 (1999).

[5] C. Vockenhuber, I. Dillmann, M. Heil, F. Käppeler, N. Winckler, W. Kutschera, A. Wallner, M. Bichler, S. Dababneh, S. Bisterzo, and R. Gallino, Phys. Rev. C **75**, 015804 (2007).

[6] M. Heil, F. Käppeler, E. Uberseder, R. Gallino, and M. Pignatari, Phys. Rev. C **77**, 015808 (2008).

[7] Z. Bao, H. Beer, F. Käppeler, F. Voss, K. Wisshak, and T. Rauscher, At. Data Nucl. Data Tables **76**, 70 (2000).

[8] M. Heil, S. Dababneh, A. Juseviciute, F. Käppeler, R. Plag, R. Reifarth, and S. O'Brien, Phys. Rev. C **71**, 025803 (2005).

[9] F. Käppeler, A. A. Naqvi, and M. Al-Ohali, Phys. Rev. C **35**, 936 (1987).

[10] V. Pronyaev, A. Mengoni, and A. Carlson, Technical Report No. INDC(NDS)-0540, IAEA Vienna, (2008).

[11] H. Beer and F. Käppeler, Phys. Rev. C **21**, 534 (1980).

[12] G. Feinberg, M. Friedman, A. Krasa, A. Shorl, Y. Eisen, D. Berkovits, D. Cohen, G. Giorginis, T. Hirsh, M. Paul, A. J. M. Plompen, and E. Tsuk, Phys. Rev. C **85**, 055810 (2012).

[13] S. Röttger, R. Böttger, F. D. Brooks, A. Buffler, J.-P. Meulders, R. Nolte, F. D. Smit, and F. Wissmann, in *Proceedings of the Fourth International Workshop on Nuclear Fission and Fission-Product Spectroscopy* AIP Conference Proceedings, Vol. 1175, (American Institute of Physics, Melville, NY, 2009), p. 375.

[14] H. J. Brede, M. Cosack, G. Dietze, H. Gumpert, S. Guldbakke, R. Jahr, M. Kutschera, D. Schlegel-Bickmann, and H. Schlermann, Nucl. Instrum. Methods **169**, 349 (1980).

[15] J. Apostolakis, Technical Report, CERN, GEANT library [http://wwwinfo.cern.ch/asd/geant/], (1993).

[16] ^{6}Li$(n,\alpha)^3$H cross section (2006), ENDF/B-VII, standards sublibrary [http://www-nds.iaea.org/standards/].

[17] R. Reifarth, M. Heil, F. Käppeler, and R. Plag, Nucl. Instr. Meth. A **608**, 139 (2009).

[18] S. Schmidt, Master thesis, Goethe Universität Frankfurt, 2011; [http://nbn-resolving.de/urn/resolver.pl?urn:nbn:de:hebis:30-109005].

[19] S. Badikov, C. Zhenpeng, A. D. Carlson, E. V. Gai, G. M. Hale, F. J. Hambusch, H. M. Hofmann, T. Kawano, N. M. Larson, V. G. Pronyaev, D. L. Smith, S. Y. Oh, S. Tagesen, and H. Vonach, Technical Report, IAEA Vienna [http://www-nds.iaea.org/standards/] (2007).

[20] C. Lederer *et al.* (n_TOF collaboration), Phys. Rev. C **83**, 034608 (2011).

[21] P. Schillebeeckx (private communication).

[22] A. Carlson, V. G. Pronyaev, F. J. Hambusch, F. Käppeler, W. Mannhart, A. Mengoni, R. O. Nelson, P. Talou, S. Tagesen, and H. Vonach, J. Korean Phys. Soc. **59**, 1390 (2011).

[23] R. Reifarth, M. Heil, F. Käppeler, F. Voss, K. Wisshak, F. Bečvář, M. Krtička, R. Gallino, and Y. Nagai, Phys. Rev. C **66**, 064603 (2002).